ChemElectroChem

Chemistry Europe
European Chemical Societies Publishing
ChemElectroChem

RESEARCH ARTICLE OPEN ACCESS

Electrochemical Reduction of Nitrate to Ammonia on Transition-Metal Sputtered Copper Foams

Sabita Bhandari[1] | Nick Hausen[2] | Xin Wei[1] | Michael Noyong[1] | Regina Palkovits[2,3] | Ulrich Simon[1]

[1]Chair of Inorganic Chemistry and Electrochemistry, Institute of Inorganic Chemistry, RWTH Aachen University, Aachen, Germany | [2]Chair of Heterogeneous Catalysis and Technical Chemistry, Institute of Technical and Macromolecular Chemistry, RWTH Aachen University, Aachen, Germany | [3]Institute for a Sustainable Hydrogen Economy, Forschungszentrum Jülich, Jülich, Germany

Correspondence: Sabita Bhandari (sabita.bhandari@ac.rwth-aachen.de) | Ulrich Simon (ulrich.simon@ac.rwth-aachen.de)

Received: 25 April 2026 | **Revised:** 2 July 2026 | **Accepted:** 7 July 2026

Keywords: ammonia | heterogeneous catalysis | nitrate reduction | thin films | transition metals

ABSTRACT

The electrochemical nitrate reduction to ammonia (eNO_3RR) is an important step toward sustainable ammonia synthesis. Despite a few challenges in securing sufficient nitrate sources for commercial scale production of ammonia, a key current focus is the search for a cost-effective yet highly active catalyst. Here, we present physical vapor deposition as a quick and straightforward technique for producing a thin layer of cobalt deposits on copper foam which shows significant performance (95% FE_{NH3}) for eNO_3RR. The superior performance of the Co–Cu foam is proposed to arise from the synergistic impact of Co–Cu on the direct reduction of NO_3^- to NH_3, coupled with the subsequent reduction of NO_2^- produced on Cu sites.

1 | Introduction

Ammonia (NH_3) is one of the most important chemicals for fertilizers, pharmaceuticals, textiles, refrigeration, and various other purposes. The total global NH_3 production was reported to be higher than 182 million tonnes in 2021 [1]. Haber Bosch is still the main commercial production process for NH_3 utilizing nitrogen (N_2) and hydrogen (H_2) at 300–550 °C and 200–350 atm in the presence of an iron catalyst [2]. As reported by International Energy Agency, 2021, this process accounts for 1.3% of total energy system-related carbon dioxide (CO_2) emissions majorly caused by hydrogen production from fossil sources [1]. Given the challenges of climate change and global warming, any process, such as Haber Bosch, hugely contributing to the CO_2 emission is a matter of concern. As an energy efficient alternative to Haber Bosch process, electrochemical reduction of atmospheric nitrogen to ammonia (eNRR) at room temperature and pressure has been widely studied in the last decade. When compared to the Haber Bosch process, eNRR technology is reported to save over 20% on energy and be driven by clean and renewable energy sources [3]. However, almost all these attempts only allow producing insignificant quantity of ammonia [4–7] as the overall process is hindered by kinetic and thermodynamic obstacles [8, 9].

Considering the fact that eNRR is not efficacious for commercial scale NH_3 production, in recent years, an additional electrochemical method for NH_3 production is vigorously being studied, which is electrochemical reduction of nitrate to NH_3 (eNO_3RR) [10] or related derivatives such as urea [11]. Nitrate is a common water pollutant arising from both natural and human activities and poses a greater risk to human health and aquatic life [12, 13]. The eNO_3RR presents a potentially green and energy-efficient approach that delivers dual benefits of removing nitrate from water bodies and simultaneously producing industrially valuable NH_3.

$$NO_3 + 9H^+ + 8e^- \rightarrow NH_3 + 3H_2O,\ E^0 = -0.12\ \text{V vs. SHE} \quad (1)$$

The overall eNO_3RR involves an $8e^-$ transfer (see Equation (1)), which results in slow reaction kinetics [14]. Although eNO_3RR is a multistep multielectron reaction, it is more facile compared to eNRR ($6e^-$ transfer) due to the weaker bond strength of N—O than

N≡N and the higher solubility of nitrate ions in aqueous electrolyte compared to that of nitrogen [15–17]. Nevertheless, there is a high competition with hydrogen evolution reaction (HER) that occurs in a similar potential window [18–20]. Additional by-products, such as N_2, nitrite (NO_2^-), hydroxylamine (NH_2OH), etc., are frequently reported [18–24]. Therefore, the selectivity and efficiency of the overall process is greatly reduced. In this regard, the development of a highly selective, active, and stable electrocatalyst for eNO_3RR is essential.

Both noble and non-noble metals have been extensively studied for their electrocatalytic nitrate reduction properties. Precious metal-based catalysts, such as ruthenium nanoclusters (nearly 100% ammonia selectivity) [25], copper-supported rhodium cluster (Faradaic efficiency, FE of ∼93%) [26], strained Ru nanostructures (100% FE), with a production rate of 5.56 mol g_{cat}^{-1} h^{-1} [25] are reported. Optimized bimetallic nanocrystal alloy $Pd_{74}Ru_{26}$ is reported to show ∼100% FE over a wide potential window from 0.1 to −0.3 $V_{versus\ RHE\ (reversible\ hydrogen\ electrode)}$ at a low nitrate concentration of 32.3 mM [27]. Dima et al. suggested that the electrocatalytic activity for eNO_3RR for metals follows the order; Rh > Ru > Ir > Pd and Pt [28]. The optimized RuFe-NC catalyst is claimed to achieve 100% FE with a high production rate of 0.83 mg h^{-1} mg_{cat}^{-1} at −0.1 $V_{versus\ RHE}$, outperforming most reported catalysts [29]. Besides, photodeposited Ru nanoclusters on TiO_2 nanotubes have been reported to show ammonia production rates of ≈600 μg $h^{-1}cm^{-2}$ and a FE of >90.0% [30].

On the nonprecious metal-based catalyst side, Cu, Fe, Co, and binary metal-based catalysts have been reported with excellent performance for eNO_3RR [31–36]. Among them, Cu is considered one of the best nonprecious metal catalysts for eNO_3RR. Herein, CuO nanowire arrays are reported to be efficient for eNO_3RR with 95.8% FE and an ammonia selectivity of 81.2% [37]. Au_1Cu (111) single-atom alloys with isolated Au atoms and adjacent Cu vacancies are reported to exhibit FE of 98.7% with a production rate of 555 μg h^{-1} cm^{-2} at 0.2 $V_{versus\ RHE}$ [38]. CoO/Cu foam produced via electrodeposition and subsequent calcination is demonstrated to achieve an NH_3 production of 4.3 mg cm^{-2} h^{-1} with 96.7% FE, surpassing Cu foam (1.2 mg cm^{-2} h^{-1}) and CoO/Ni foam (1.3 mg cm^{-2} h^{-1}) electrodes [39]. A heterostructured Cu_2O/Co_3O_4@NC catalyst is demonstrated to be a good eNO_3RR catalyst showing 96.75% FE, NH_3 selectivity of 87.38%, and a production rate of 1.46 mmol cm^{-2} h^{-1} at −0.45 $V_{versus\ RHE}$ [40]. A dual-site catalyst made up of atomically dispersed Cu atoms anchored on defective NiFe-LDH is reported to show 95.2% FE and 2.08 mg cm^{-2} h^{-1} NH_3 yield at low nitrate concentration of 100 mg-NL^{-1} [41]. Ti-foil, on the other hand, is shown to display 82% FE at a working electrode potential of −1 $V_{versus\ RHE}$ [42]. Besides, Fe-SAC catalysts with single Fe atoms dispersed on the porous carbon matrix are known to show ∼75% FE at −0.66$V_{versus\ RHE}$ and a production rate of 0.46 mmol cm^{-2} h^{-1} at −0.85 $V_{versus\ RHE}$ [32].

Given the demonstrated electrocatalytic potential of transition metal-based catalysts for eNO_3RR, this work focuses on copper, cobalt, and nickel for their electrocatalytic performance. These metals are earth-abundant and cheaper (Co, $25.533 per pound), (Ni, $8.0535 per pound), (Cu, $5.8342 per pound) compared to precious metals such as Ru ($910.00 per ounce) and Rh ($10,100.00 per ounce) according to the current market price as of January 17th, 2026. Since sustainable energy conversion systems necessitate the use of sustainable materials, these metals represent an excellent choice as catalysts for eNO_3RR with subsequent optimization if needed. The starting material for the current project was commercial Cu foam, which was then sputtered with Co and Ni for 2 min. To deposit a thin layer of Co or Ni onto Cu foam and promote synergistic Co–Cu and Ni–Cu effects, magnetron sputtering for 2 min was selected. The Co- and Ni-sputtered Cu foams are referred to as Co–Cu foam and Ni–Cu foam, respectively, from here onwards. The motivation was to understand and analyze the impact of Co–Cu and Ni–Cu incorporation toward eNO_3RR performance compared to that of bare (commercial) Cu foam. Magnetron sputtering, a form of physical vapor deposition, was used to prepare thin metal deposits on Cu foam as this technique is known to produce a highly uniform and conformal coating with high purity on the porous 3D surface such as copper foam [10]. Electrodeposition on the other hand could be another economic method for metal deposition; however, for complex, rough, and porous copper foam, electrodeposition is likely to be nonuniform, which justifies the use of sputtering [43]. Besides, in sputtering process, energetic atoms are reported to coat both outer and inner surfaces of the Cu foam more uniformly, leading to a more consistent thin film across the foam structure. Additionally, sputtered layers are reported to possess strong adhesion due to an atomic level bonding, exhibiting higher oxidation resistance, and are stable under harsh electrochemical conditions such as eNRR as recently demonstrated [44–46].

2 | Results and Discussion

2.1 | Thickness of Metal Deposit via Sputtering on a Model System

Characterizing film thickness directly on porous copper foam is challenging due to the substrate's high porosity and irregular topography. These factors make it difficult to distinguish discrete layers and hence obtain reliable cross-sectional measurements. To compensate this limitation, a model system (Si wafer) was utilized as a flat model substrate. Cobalt was sputtered onto the Si wafer for 1, 2, 3, and 8 min, respectively, under the same conditions that were used for sputtering Cu foam with the Co- and Ni-targets. Cross-sectional scanning electron microscopy (SEM) analysis of the model system showed average film thicknesses of ∼31, ∼62, ∼87, and ∼210 nm for sputtering times of 1, 2, 3 and 8 min, respectively (see Figure S5). The thickness of deposit was found to increase with sputtering time, indicating a direct correlation between deposition time and film thickness. The linear fit for the measured thickness is shown in Figure 1, which suggests a strong linear relationship between sputtering time and film thickness with a Pearson correlation coefficient of $R^2 = 0.999$. From this observation, the thickness of metal deposit on Cu foam could be assumed to be tentatively around 62 nm for 2 min sputtering time.

2.2 | Contact Angle

The as-purchased copper foam shows a contact angle of 98° on water drop, which gets slightly increased to 106° and 112° on

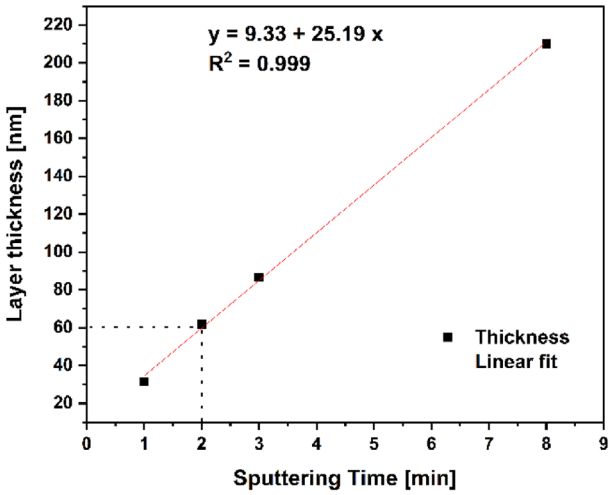

FIGURE 1 | Correlation of sputtering time and thickness of deposit on model system of Si wafer.

Ni–Cu and Co–Cu foam, respectively (Figure 2). This suggests that deposition of cobalt and nickel on the copper surface slightly increases the hydrophobicity of Cu foam surface, reducing its wettability. A similar behavior of a cobalt-doped copper surface has been reported by W. Darenfad et al. as well [47]. Such behavior might not always be favorable for electrochemical performance in aqueous medium.

2.3 | X-Ray Diffraction

To confirm the crystalline phases formed on Co- and Ni-sputtered Cu foam, X-ray diffraction (XRD) measurement were performed. The XRD patterns are shown in Figure S6, where it is observed that the XRD patterns for all the samples overlap, and no distinct features attributable to the deposited metal (Co and Ni) are observed, indicating that the Bragg reflexes are dominated only by Cu. We attribute the absence of Co- or Ni-related XRD peaks to the very thin Co- or Ni-layer deposited on the Cu foam (~62 nm), as such a thin deposit is below the detection threshold of XRD. Nevertheless, the absence of detectable Co and Ni Bragg reflexes in XRD could also be consistent with nanoparticle formation, phase segregation, or the presence of small clusters of the sputtered metals, any of which may equally account for the lack of apparent reflexes in the XRD patterns. Interestingly, an additional peak is observed at around 2θ of 19° for the Co–Cu foam. According to the literature, neither metallic Cu nor metallic Co is expected to show a diffraction peak at around 2θ of 19° under Cu Kα radiation [48–51]. Although Co_3O_4 can exhibit a low-angle reflection around 19°, the absence of characteristic peaks for spinel Co_3O_4 approximately at 31.3°, 36.8°, 59.4°, and 65.2° [52] in XRD pattern of Co–Cu foam suggests that the peak around 19° cannot be confidently assigned to Co_3O_4. Since we could not assign this peak to any phase as per the reference database, its origin remains inconclusive, and we tentatively attribute it to surface contamination.

2.4 | Scanning Electron Microscopy–Energy-Dispersive X-Ray Analysis

The SEM images show that Cu foam has a highly interconnected ligaments and porous structure with pore sizes of tens of micrometers across (Figure 3a,b). When cobalt and nickel are sputtered on the copper foam, as shown in Figure 3c,d, the surface shows thin stacked layers that appear to peel off from the substrate surface creating a terraced morphology with smooth surfaces and sharp edges at the micrometer scale. The cracks and delamination suggest a poor adhesion to the substrate. Although this is not an ideal result, it is a common phenomenon in thin-film deposition techniques, including Magnetron sputtering. Such cracking arises from residual stress, thermal mismatch, and limited interfacial adhesion [53–55]. We also assume that surface contamination may have contributed, since commercially available copper foam was used directly without any prior surface treatment. Elemental mapping confirms a relatively uniformly distributed Co and Ni on the surface of the Cu foam electrode (Figure 3e,f).

2.5 | X-Ray Photoelectron Spectroscopy

X-ray photoelectron spectroscopy (XPS) characterization was performed to elucidate the surface composition and chemical state of the samples before and after eNO_3RR performance tests. Figure 4a–c shows the $2p_{3/2}$ and $2p_{1/2}$ core-level peaks for Cu foam, Co–Cu foam, and Ni–Cu foam samples before (blue line) and after (red line) electrochemical tests. The $2p_{3/2}$ peak of the bare Cu foam before eNO_3RR tests (Figure 4a) exhibits two components: one centered at 932.4 eV and other one at 934.4 eV. As the observed binding energy (BE) is within the range of values reported in the literature, we assume that the first peak at 932.4 eV corresponds to metallic Cu(0) or Cu_2O (Cu^+) and the other one at 934.4 eV to CuO (Cu^{2+}) [56–59]. As the $2p_{3/2}$ peak of Cu(0) or Cu_2O (Cu^+) differs by only 0.1 eV and cannot be

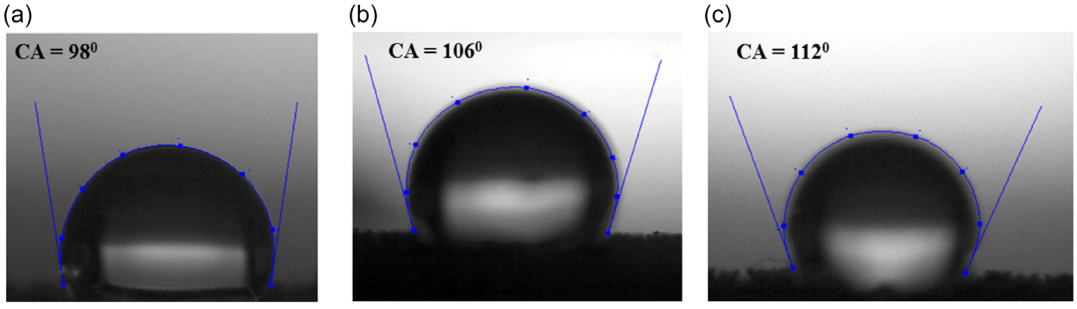

FIGURE 2 | Contact angle measurement on (a) Cu foam, (b) Ni–Cu foam, and (c) Co–Cu foam.

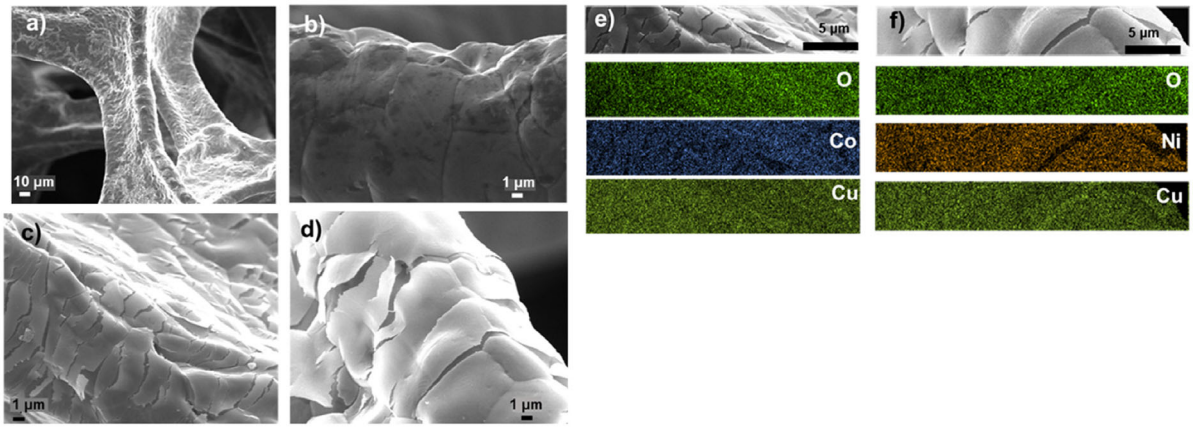

FIGURE 3 | SEM images (a) Cu foam (10 μm); (b) Cu foam (1 μm); (c) Co–Cu foam (1 μm); (d) Ni–Cu foam (1 μm); and (e,f) Elemental mapping of Co–Cu foam and Ni-Cu foam.

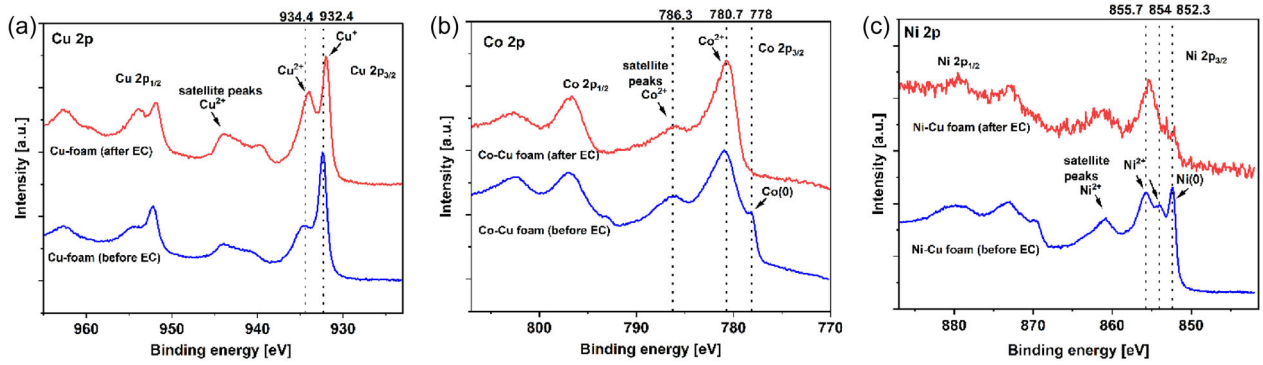

FIGURE 4 | XPS spectra of (a) Cu 2p of Cu foam, (b) Co 2p of Co–Cu foam, and (c) Ni 2p of Ni–Cu foam before (blue line) and after (red line) eNO_3RR performance analysis.

distinguished from Cu $2p_{3/2}$ peaks, we have extracted and analyzed Cu LMM Auger peaks from XPS survey spectra (Figure S7) [56]. The modified Auger parameter ($\alpha' = 1849.0$ eV, Figure S7a) and a peak at 570.1 eV (Figure S7b) characteristic of Cu_2O (Cu^+) reveal the existence of the chemical state of Cu^+, which is attributed to rapid surface oxidation during air exposure prior to XPS measurements [59, 60].

Besides, in Figure 4a, shakeup satellite peaks are observed at higher BE to the main $2p_{3/2}$ and $2P_{1/2}$ peaks, first in the range from 939.7 to 944 eV and another centered at 962.40 eV. These satellite peaks indicate the presence of CuO (Cu^{2+}) [60, 61]. These observations demonstrate that the Cu foam is surface oxidized, resulting in the formation of CuO or Cu_2O. Postelectrochemical characterization on Cu foam shows a relative increase in the intensity of the peaks at 934.4 eV, indicating an increased contribution of oxides species relative to the metallic states compared to the samples before electrochemical test. As the electrochemical protocol involved reductive conditions, surface reduction of Cu foam was anticipated considering a decrease in the oxygen-containing species. Nevertheless, we attribute the observed surface oxidation to postelectrochemical exposure of Cu foam to atmospheric oxygen, leading to reoxidation of the surface.

In Figure 4b, Co 2p spectra are shown, where $2p_{3/2}$ transition is characterized by a main peak and a satellite on the higher BE side. For Co–Cu foam before eNO_3RR, a small peak at 778 eV, a broad peak centered at 780.7 eV, and a satellite peak at nearly 786.3 eV are observed. The assignment of Co $2p_{3/2}$ peaks is based on literature, with a peak at 780.7 eV assigned to Co^{2+} in CoO and a satellite peak centered at nearly 786.3 eV to Co^{2+} (CoO) [62–65]. A peak at 778 eV is an indication of metallic Co(0) [65, 66]. The $2p_{3/2}$ features after EC measurements show a loss of metallic Co peak at 778 eV, indicating either a further oxidation of the surface after eNO_3RR following exposure to atmosphere as in the case of Cu foam or a loss of Co metal deposit after eNO_3RR. This was evaluated by comparing the Cu $2p_{3/2}$ peaks on Co–Cu foam both before and after electrochemical tests (see Figure S8a). The more pronounced Cu 2p features on Co–Cu foam after eNO_3RR indicate leaching of Co deposits during electrochemical tests.

The $2p_{3/2}$ peaks of Ni 2p spectra on Ni–Cu foam before eNO_3RR (Figure 4c, blue curve) show a peak at 852.3 eV, indicating a Ni(0) metallic state along with NiO at 854 eV and $Ni(OH)_2$ at 855.7 eV [2, 66]. The formation of thin layer of NiO and $Ni(OH)_2$ on the surface of Ni with an exposure to atmospheric moisture is reported in the literature [67]. The loss of these Ni features on the sample after electrochemical tests indicates a significant leaching of the Ni deposit from the surface of Cu foam during eNO_3RR. This can be visualized more on the Cu 2p spectra of Ni–Cu foam before and after eNO_3RR, where Cu foam 2p spectra

are more clearly visible on the Ni–Cu foam sample after electrochemical tests (see Figure S8b).

The O 1s XPS spectra of Cu foam, Co–Cu foam, and Ni–Cu foam are shown in Figure 5 in a consistent layout, with the lower spectrum in each panel (blue curve) corresponding to the pristine (before eNO_3RR) sample. Proper deconvolution of the O 1s spectra is shown in Figure S9 of the Supporting Information. The dominant O 1s component at BEs around ~529.5 to 530.0 eV is attributed to lattice oxygen in metal–oxide environments [68]. A secondary contribution on the high BE side of the main peak (>~530 eV) is assigned to oxidized surface species, primarily associated with oxides and/or hydroxylated species [68]. For example, the pristine Cu foam shows a shoulder at BEs around ~529.0 to 531.0 eV, which can be assigned to lattice oxygen in metal–oxide environments. Additional contributions at higher BEs (~531.5 to 533 eV) may originate from adsorbed oxygen-containing species such as hydroxyl groups, carbonates, or residual surface contamination, which are commonly observed in air-exposed samples. In contrast to the pristine samples, the O 1s spectra recorded after eNO_3RR tests show a pronounced change in spectral shape. Notably, a significant decrease is observed in the component at BEs around ~529.5 to 530.0 eV previously assigned to lattice oxygen (see Figure S9). The O 1s signal is now dominated by a single, more symmetric component centered around 531 eV, which is attributed to hydroxylated/adsorbed oxygen species, including surface hydroxyl groups and adsorbed water, as well as possible contributions from hydroxylated Ni/Co (oxy)hydroxide species formed under alkaline electrochemical conditions. However, due to the strong overlap of O 1s BEs, a clear distinction between Ni/Co oxide and hydroxide phases cannot be reliably made.

2.6 | Electrochemical Nitrate Reduction to Ammonia Performance Analysis

The electrochemical performance of the commercial Cu foam along with Co–Cu foam and Ni–Cu foam was tested in 0.1 M KOH with 0.016 M (1000 ppm) NO_3^- in the potential range from 0.475 V to −0.359 $V_{versus\ RHE}$ with cyclic voltammetry experiment (see Figure 6, red curve). All the experiments were performed with IR compensation at 80%. The background current generated mostly by the competitive HER was measured by running the same experiments in the absence of NO_3^- (see Figure 6, black curve). Considering the fact that, in the presence of NO_3^-, an unavoidable background current may still occur, we assume that the red curve includes contributions from both reactions, eNO_3RR and HER. As shown in Figure 6, Cu foam appears to perform poorly for both eNO_3RR and HER as shown by low current responses within the applied potential window for both electrolytes with NO_3^- and without NO_3^-. On the other hand, for Ni–Cu foam, even without NO_3^- in the electrolyte, the current response is very high and comparable to that when NO_3^- is present. This observation suggests that Ni–Cu foam is a good HER catalyst instead of eNO_3RR catalyst. In contrast, for Co–Cu foam, an enhanced current response is observed for eNO_3RR (when NO_3^- is present) compared to HER (when NO_3^- is absent), indicating its more favorable kinetics toward eNO_3RR.

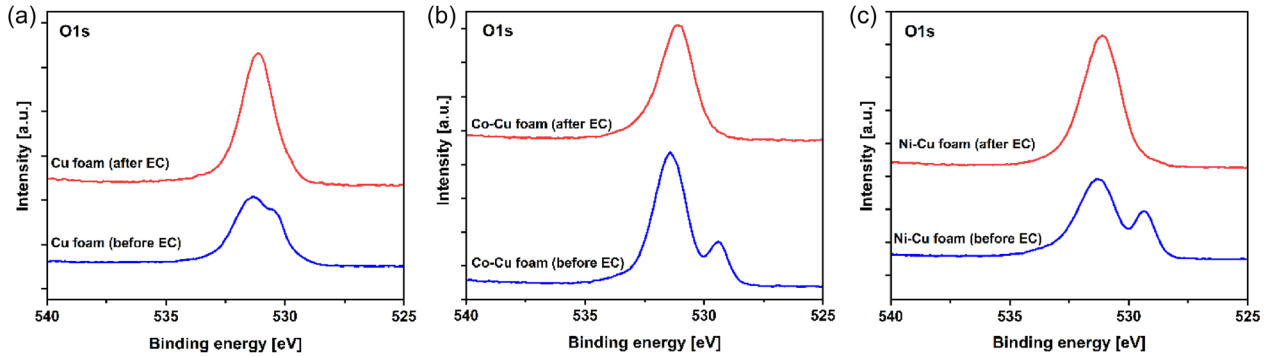

FIGURE 5 | Comparison of O 1s spectra on (a) Cu foam, (b) Co–Cu foam, and (c) Ni–Cu foam before (blue line) and after (red line) eNO_3RR performance analysis.

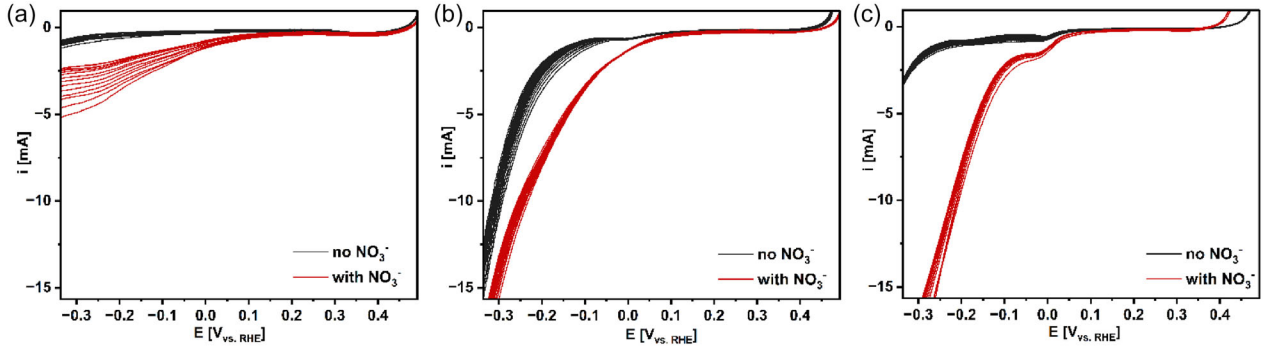

FIGURE 6 | Electrochemical performance of (a) Cu foam, (b) Ni–Cu foam, and (c) Co–Cu foam in 0.1 M KOH with and without NO_3^-.

A reduction peak around 0 $V_{versus\ RHE}$ is observed on Co–Cu and Ni–Cu, especially when NO_3^- is absent. As this peak is present in both Co–Cu and Ni–Cu in the absence of NO_3^-, we assume it to mainly reflect a surface-related change on Ni and Co, for example, surface oxide reduction. XPS analysis shows the presence of surface oxides on both Co–Cu foam and Ni–Cu foam. Besides, in alkaline media, Ni and Co surfaces are reported to have oxyhydroxide/oxide species, and the cathodic scan can reduce these layers to metallic states, giving rise to a reduction peak [69]. When NO_3^- is present, the peaks may be suppressed because the surface is modified by NO_3^- adsorption as observed in Ni–Cu foam or they may shift to a new potential as observed in Co–Cu foam. In Co–Cu foam, a new peak appearing in a similar potential range in the presence of NO_3^- could represent either (i) a modified surface with a new reduction potential for the reduction of surface oxides to the metallic state, or (ii) the initial reduction of NO_3^- to NO_2^-, as reported in previous literature [39, 70].

In order to better understand the impact of Co and Ni incorporation on Cu, electrochemical impedance spectroscopy (EIS) data and their equivalent circuit fittings have been included in the Supporting Information (Figure S11). Although the contact angles (Figure 2) increase slightly following Co or Ni deposition on the Cu surface, indicative of reduced surface wettability, the charge transfer resistance (R_{ct}) is significantly decreased relative to bare Cu foam. This suggests that the introduction of Co and Ni on Cu-surface actually facilitates electron transfer, as reflected in the lower R_{ct} values. These results collectively indicate that the enhanced electrocatalytic performance of the catalysts is governed primarily by improved charge transfer kinetics rather than by surface wettability only. In all these catalysts, when NO_3^- is present, reaction appears to start, as indicated by a sharp increase in reductive current at a slightly more positive potential compared to that in the absence of NO_3^- in the electrolyte (black vs. red curve in Figure 6). This is an indication that less overpotential is needed for eNO_3RR compared to HER. Ni being a good HER catalyst [71, 72] shows a minor difference on the onset potential for HER and eNO_3RR, while a significant difference is seen on the Co–Cu foam catalysts, further suggesting that Co–Cu foam is more suitable for eNO_3RR than Cu foam and Ni–Cu foam. In order to further elucidate the eNO_3RR performance and the reaction kinetics of the catalysts, Tafel slopes calculated from the LSV curves (Figure 6, red curves) are compared in Figure 7a. For Co–Cu foam, the slopes are lower (178 mV/dec) compared to the other two counterparts (Ni–Cu foam; 266 mV/dec and Cu foam; 569 mV/dec) in the potential range from −0.05 V to −0.15 $V_{versus\ RHE}$. These above findings suggest that Co–Cu foam has more favorable eNO_3RR kinetics than the other samples as less energy (overpotential) is required to change current density by one order of magnitude [73]. Additionally, Tafel slopes for eNO_3RR and HER are compared for Co–Cu foam across two distinct potential regions (Figure 7b). In the low overpotential region (less negative potentials), lower Tafel slopes are observed for eNO_3RR (226 mV/dec) than that for HER (511 mV/dec), indicating more favorable eNO_3RR kinetics in that potential window. In contrast, at high overpotential region (more negative potentials), the trend is reversed, with HER displaying lower Tafel slopes (146 mV/dec) than eNO_3RR (381 mV/dec).

A direct quantitative comparison of eNO_3RR performance was made based on the FE and production rate for NH_3 in all these catalysts (Figure 8). For determining these quantities, chronoamperometry (CA) experiment with constant potential of −0.359 $V_{versus\ RHE}$ for 30 min was run and the current response was recorded as a function of time. The electrolyte was collected after CA experiment and then analyzed with UV–Vis spectroscopy for quantifying the concentration of NH_3, NO_2^-, and NO_3^-. FE and production rates of NH_3 were then calculated using following equations [17];

$$\text{FE}\,\% = \frac{n \times 96,485 \times C \times V}{M \times Q} \times 100\%$$

$$\text{Production rate} = \frac{C \times V}{t \times S}$$

where n is the number of electrons transferred, C is the concentration of NH_3 mg L^{-1}, V is the volume of electrolyte, M is the molar mass of NH_3, Q is the charge consumed, t is the reaction time, and S is the surface area of electrode. At least three measurement data were used for determining the mean value of FE (with standard error) shown in Figure 8. As shown in Figure 8a, Co–Cu foam shows a FE nearly around 80%, while Cu foam shows around 25% and Ni–Cu foam shows FE around 40%. Here, the synergistic incorporation of Ni and Cu did not

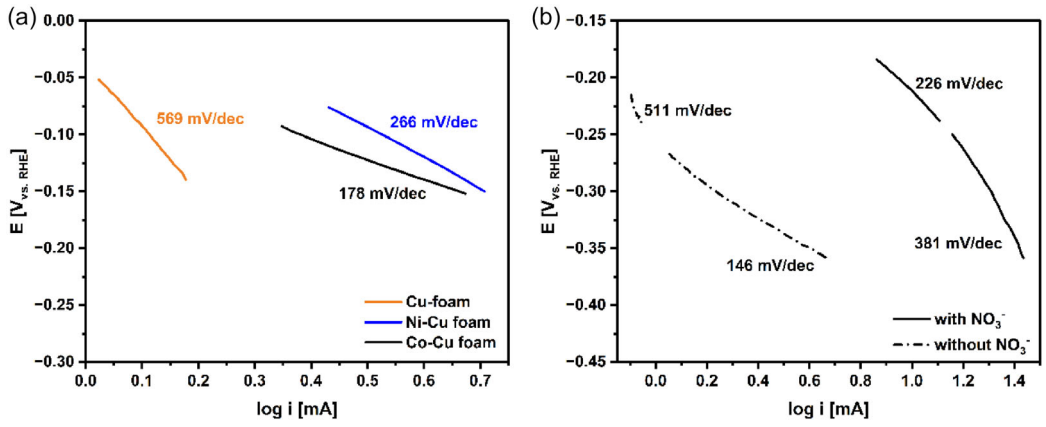

FIGURE 7 | Tafel slopes of (a) Cu foam, Co–Cu foam & Ni–Cu foam for eNO_3RR and (b) comparison of Tafel slopes for eNO_3RR and HER on Co–Cu foam in 0.1 M KOH.

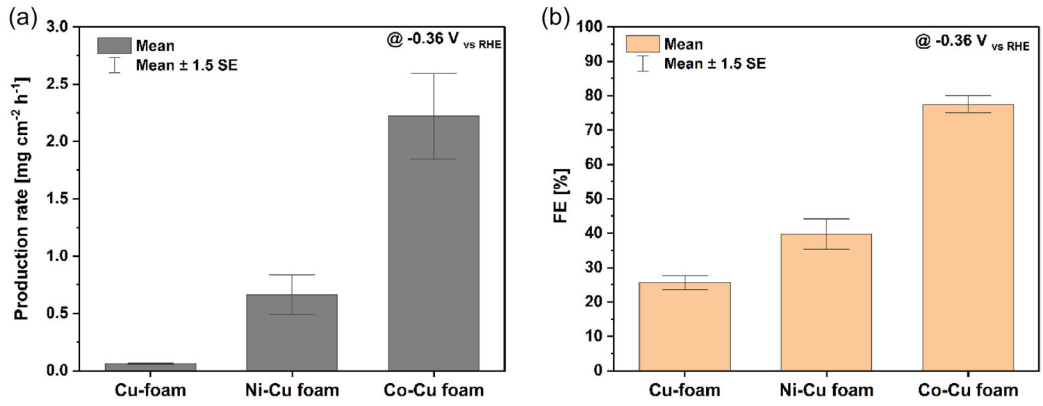

FIGURE 8 | Comparison of (a) production rate and (b) FE for NH_3 on different catalysts in 0.1 M KOH with 0.016 M NO_3^- @ −0.359 $V_{versus\ RHE}$.

significantly enhance electrochemical nitrate reduction performance, unlike findings reported in prior literature [74, 75]. This result suggests that at the potential of around −0.359 V, Co–Cu foam exhibits superior electrocatalytic performance for eNO_3RR compared to both blank Cu foam and Ni–Cu foam. Similar conclusion is suggested by production rate as well, where Co–Cu foam shows highest production rate among all these catalysts (Figure 8b). Undoubtedly, the production rate observed here is lower compared to the values reported in literature. For example, CoO/Cu foam is reported to show a NH_3 yield rate of 4.3 mg cm^{-2} h^{-1} at −1.2 $V_{versus\ Ag/AgCl}$ for 0.04 M NO_3^- concentrations [39] while Fe-doped TiO_2 is reported to show maximum NH_3 yield of 5.95 mg cm^{-2} h^{-1} at 0.7 $V_{versus\ RHE}$ for 0.1 M NO_3^- concentrations [76]. The bimetallic TTA-TPH CuCo COF has shown high NH_3 yield of 20.8 mg cm^{-2} h^{-1} at 0.75 $V_{versus\ RHE}$ in 0.3 M NO_3^- concentrations [77].

Interestingly in the literature, it has also been explicitly demonstrated that the NH_3 production (yield) rates are directly dependent on the concentration of NO_3^- in the electrolyte [42, 78, 79]. The low production rate of NH_3 observed for Co–Cu foam compared to literature data could also be due to the low nitrate concentration in the electrolyte and a lower overpotential. In order to prove that, we ran CA experiments at constant potential of −0.359 V for 30 min in 0.05 M NO_3^- concentration in contrast to 0.016 M NO_3^- (1000 ppm) concentration used for all previous experiments. A plot of current response against time is shown in Figure 9, which shows nearly a 2.5-fold higher current response for higher NO_3^- concentration. The electrolyte was then evaluated with UV–Vis and the concentration of NH_3 was determined. The NH_3 production rate of the Co–Cu foam in 0.05 M NO_3^- reached 7.82×10^3 μg cm^{-2} h^{-1}, approximately three times higher than that at 0.016 M NO_3^-, whereas the FE at 0.05 M NO_3^- (79.3%) showed no substantial improvement.

As Co–Cu foam is more active for eNO_3RR, major focus is placed on this catalyst, and a range of potentials were evaluated to determine the FE for NH_3. For this reason, CA experiments were run at various potentials for 30 min in 0.1 M KOH with 0.016 M NO_3^- and the resulting current response over measurement time is recorded (see Figure S8). A comparison of FE and production rates for NH_3 at various applied potentials for Co–Cu foam is shown in Figure 10. As shown in Figure 10a, the highest FE of 95% is observed at −0.222 $V_{versus\ RHE}$, which decreases when

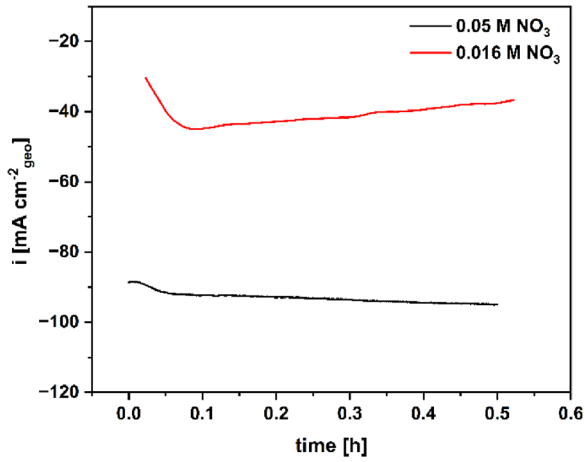

FIGURE 9 | A comparison of current response on Co–Cu foam in 0.1 M KOH with NO_3^- concentration of 0.016 and 0.05 M.

the applied potential is shifted either positively or negatively. At potentials between −0.20 and −0.24 $V_{versus\ RHE}$, the Tafel slope for eNO_3RR is lower than that for HER, suggesting that eNO_3RR exhibits favorable kinetics in this potential window (Figure 7b). As further shown in Figure 10a, this potential range shows the best FE for NH_3 with maximum value of 95% FE at −0.222 $V_{versus\ RHE}$. Beyond this potential range, FE for NH_3 declines probably due to increasing HER competition at higher cathodic overpotentials. The combination of favorable reaction kinetics of eNO_3RR identified from Tafel analysis (Figure 7b) and FE shown in Figure 10a within this potential range provides self-consistent evidence for defining it as the optimal operating potential window. However, production rates show a different trend than FE and are still higher at higher applied potentials as shown in Figure 10b. It can be inferred that the production rates are influenced by many other factors such as NO_3^- concentration, applied potential, current response, surface area of electrode, and so on, as further supported by the experiments shown in Figure 9.

In order to understand why Co addition on Cu foam improved its eNO_3RR performance, production of intermediates was considered. As suggested by various previous works, eNO_3RR undergoes multiple electron transfer steps producing a number of intermediates or side products such as NO_2^-, N_2, NH_2OH, and H_2. Many previous works have suggested NO_2^- as the universal

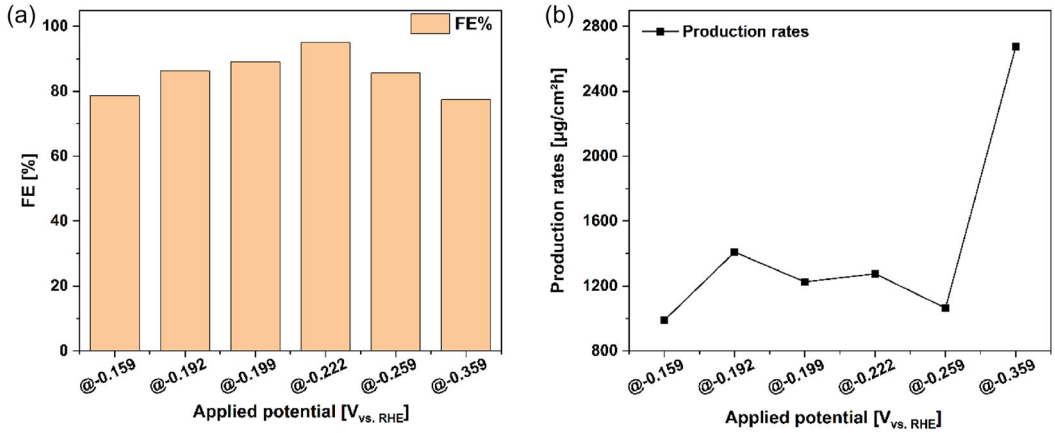

FIGURE 10 | Comparison of (a) FE and (b) production rates for NH_3 on Co–Cu foams at different potentials in 0.1 M KOH with 0.016 M NO_3^-.

first intermediate product or the major product at low overpotential region, while NH_3 is seen as the main product at high overpotential region [23, 24]. N_2 is observed as a major product at relatively low NO_3^- concentration around an applied potential of 1.17 $V_{versus\ SHE}$ [21] and NH_2OH is considered a minor intermediate in eNO_3RR pathways [22]. In addition to these, HER is the main parasitic reaction as suggested by multiple research works [18–20, 80].

In this study, the most commonly mentioned intermediate product NO_2^- [23, 24] was studied on Cu foam, Ni–Cu foam, and Co–Cu foam and presented in terms of FE in Figure 11a. Here, a number of individual samples (Sam-1 to Sam-5) of all catalysts are studied for eNO_3RR under the same conditions. The results indicate a more selective production of NO_2^- and NH_3 in nearly equal ratio on Cu foam compared to the metal-sputtered Cu foams. Here, approximately one-third of the total charge is directed toward NH_3 formation, another one-third toward NO_2^- production, and the remaining fraction is consumed in producing other intermediates/side products that cannot be detected via UV–Vis alone. The low FE for NH_3 and production of significant intermediates or side products indicate that Cu foam is a poor catalyst for eNO_3RR. Besides, deactivation of Cu-based catalysts due to aggregation and strong adsorption of NO_2^- and NO is reported in the literature, making it an poor catalyst for eNO_3RR [33, 37, 81]. Ni–Cu foam (Figure 11b) too shows low FE for NO_2^- along with low FE for NH_3 and mostly produces other intermediates or the side product, probably hydrogen.

Interestingly, Co–Cu foam, on the other hand, shows higher FE for NH_3 and significantly lower NO_2^- production compared to bare Cu foam. In the literature, it is also mentioned that Co facilitates a strong adsorption of *H and helps consecutive hydrogenation of intermediates such as NO_2^- during eNO_3RR [80, 82, 83]. Carvalho et al. utilized density functional theory (DFT) calculations to show that one of the reasons why NH_3 selectivity is high for Co, is a strong NO_2^- binding and its subsequent reduction [80]. In order to better understand this aspect, we investigated NO_2^- reduction capacity of Co–Cu foam catalysts. For this reason, electrochemical nitrite reduction activity (eNO_2RR) of Co–Cu foam is evaluated in 0.1 M KOH containing $NaNO_2$ with 0.016 M NO_2^- via CA experiment at applied potential of −0.359 $V_{versus\ RHE}$ for 30 min. The electrolyte after the electrochemical performance test is collected and evaluated for NH_3 concentration, which is then used for determining FE for NH_3. Four individual Co–Cu foam samples (Sam-1 to Sam-4) were tested under similar conditions for eNO_3RR, with the resulting FE data shown in Figure 12.

As shown in Figure 12, FE for NH_3 via eNO_2RR on Co–Cu foam reaches around 80%, demonstrating high catalytic activity for eNO_2RR. For comparative purpose, eNO_2RR performance of pure Cu foam was also evaluated, which shows a FE of around 49%. This result suggests that the Co–Cu foam facilitates the reduction of NO_2^- to NH_3 more effectively than pure Cu foam. Consequently, this enhanced catalytic activity leads to a decreased NO_2^- concentration observed and simultaneously increases the

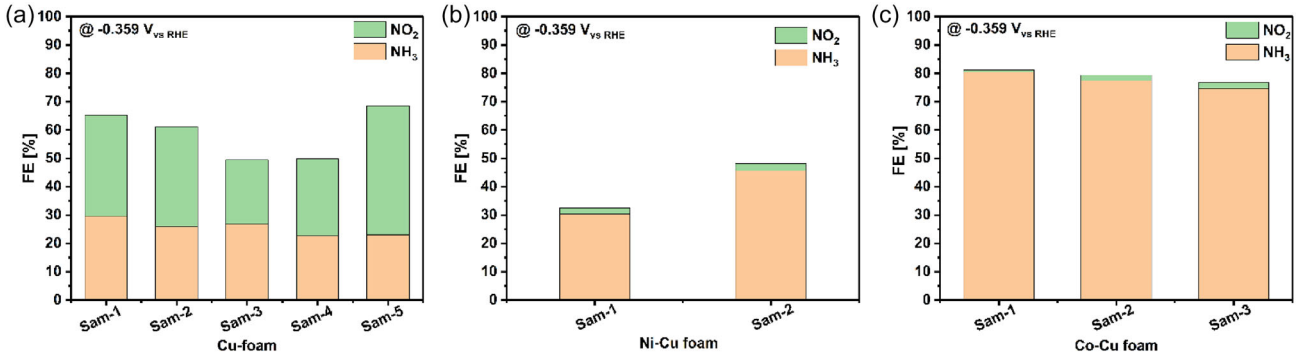

FIGURE 11 | Comparison of FE for NH_3 and NO_2^- on (a) Cu foam, (b) Ni–Cu foam, and (c) Co–Cu foams at 0.359 V$_{versus\ RHE}$ in 0.1 M KOH with 0.016 M NO_3^-.

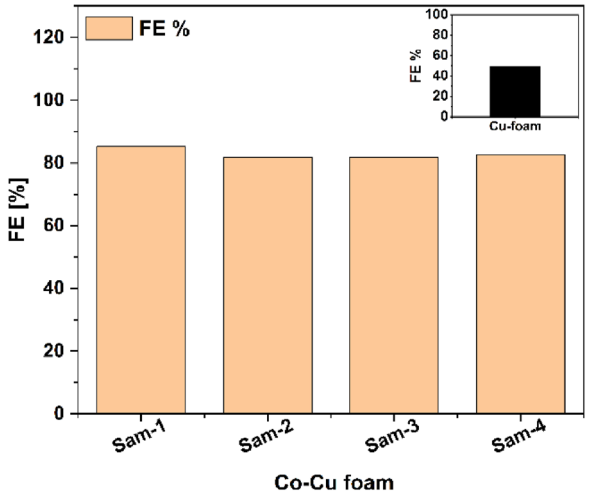

FIGURE 12 | FE_{NH3} for eNO_2RR on Co–Cu foam in 0.1 M KOH with 0.016 M NO_2^- at applied potential of $-0.359\ V_{versus\ RHE}$.

total NH_3 yield. As it is interestingly observed that a tiny quantity and a nanolayer of Co metal deposited on Cu foam is effective for enhancing electrochemical reduction of NO_3^- as well as NO_2^- to NH_3, it was also interesting to understand how the performance is affected when Cu foam is completely covered from all sides by such Co-overlayers. For this analysis, Co was sputtered for 2 min onto Cu foam on both sides. Two samples (Sam-1 and Sam-2) of the catalyst were analyzed for their eNO_3RR performance and the measured FEs (NH_3) are shown in Figure 13.

In both samples, FE is observed to reduce significantly compared to when a thin Co overlayer is deposited on only one side of Cu foam. For the double-side Co-sputtering of Cu foam, not only the two sides but also the two edges are covered, resulting in a completely Co-covered Cu foam on the exterior surface. Since Cu sites on the Co–Cu foam are equally essential for NO_2^- production (Figure 11a) as well as further reduction to NH_3 (inset, Figure 12), a completely Co-covered Cu foam surface would inherently restrict reactant access to Cu sites both on the surface and within the subsurface region spanning the depth of Co deposition (~62 nm). We therefore propose that in the case of a completely Co-covered surface, limited reactant access to Cu sites significantly reduces the overall eNO_3RR performance of Co–Cu foam. Nevertheless, the Cu remains accessible deeper inside the foam structure beyond the 62 nm penetration depth of Co deposits; however, reactant access to these regions is limited due to their position deep within the catalyst layers. Here, we propose that the spatial distribution of potential across the porous Cu foam surface plays an important role. Nonuniform spatial distribution of the applied potential across the porous structure is also a contributing factor affecting the electrochemical performance of such materials.

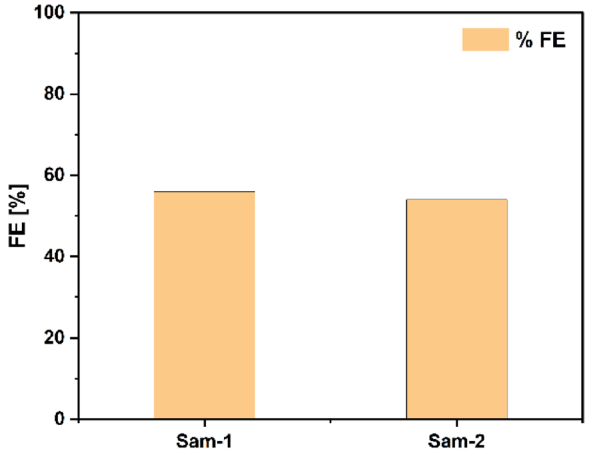

FIGURE 13 | FE_{NH3} for eNO_3RR on Co–Cu foam with Co sputtered for 2 min on each side of Cu foam.

When a certain potential is applied on a porous structure, it is not equally distributed among various sites (from the surface to deep inside the pores). Since the outer surface experiences the least Ohmic resistance while the deeper pores experience the highest, the applied potential progressively decreases from the surface to the deeper pore length [84, 85]. Therefore, the local driving force (effective potential) for a Faradaic reaction, eNO_3RR for the current context, is smaller deeper in the pores (mostly Cu sites) [84, 85]. On the other hand, Co overlayer on the surface is facing bulk electrolyte and exhibits shorter ionic as well as electronic paths; it experiences a relatively smaller Ohmic drop and therefore the effective potential on the surface is close to applied value. However, Cu sites inside the pores operate at much lower overpotential or might even get effectively inactive, and hence, the NO_2^- as well as NH_3 production is compromised. This ultimately reduces FE for NH_3 in such double-side sputtered Co–Cu foam. However, this proposed nonuniform spatial distribution of potential for our catalyst system is primarily based on our theoretical understanding and underlying assumptions used for such porous structure. Nevertheless, based on the experimental observations, we conclude that enhanced eNO_3RR performance of Co–Cu foam compared to Cu foam arises from synergistic impact of both Co and Cu, rather than from Cu sites or Co sites alone, and when either is absent or inaccessible, the performance drops accordingly.

3 | Limitations

Some limitations of the present work should be acknowledged. First, all experiments were conducted in a conventional three-electrode H-cell under natural convection without forced electrolyte flow, which introduces mass transport constraints such as diffusion of reactant and product removal from active sites that become increasingly significant over extended measurement time and make long-term stability measurements unreliable in this configuration. Second, membrane-mediated adsorption or absorption of NO_2^- and NH_3 represents a potential source of analytical uncertainty that warrants dedicated investigation beyond the scope of this study. To minimize errors arising from these limitations, experiments were intentionally kept short and products were collected after 30 min for FE analysis. Future work should employ flow cell or gas diffusion electrode configurations with controlled electrolyte convection and a well-established membrane system, which would mitigate mass transport as well as membrane-related limitations.

4 | Conclusion

A thin and uniform layer of cobalt sputtered on Cu foam can exceptionally increase the eNO_3RR performance of the commercial Cu foam. Despite the economic advantages of electrochemical deposition, magnetron sputtering is preferred for porous substrates; it ensures a more homogenous distribution of the catalytic layer across the high-surface-area internal pores of the Cu foam. It has been experimentally proven that Co sputtering for 2 min under given conditions produces a ~62-nm-thick Co overlayer on Cu foam surface and is effective for enhancing FE for NH_3 via eNO_3RR by around 3.5-fold compared to bare Cu foam.

The eNO_3RR performance of Co–Cu foam is observed to be potential dependent and maximum FE of 95% is observed at $-0.222\,V_{versus\ RHE}$ where there is minimal competition from HER and other intermediates compared to bare Cu foam and Ni–Cu foam. The superior performance of the Co–Cu foam is proposed to arise from the synergistic impact of Co–Cu on the direct reduction of NO_3^- to NH_3, coupled with the subsequent reduction of NO_2^- produced on Cu sites, as supported by the eNO_2RR results. Additionally, via the double-side sputtered Co–Cu foam, we demonstrated that Cu sites play a crucial role in enhanced eNO_3RR, as the overall performance drops when Cu sites become inaccessible. Based on all experimental results, we conclude that the enhanced performance arises from Co–Cu synergy rather than a pure contribution of either component alone in Co–Cu foam catalysts. The stability aspect of the Co–Cu foam for eNO_3RR is beyond the scope and objective of the current research work. However, dedicated stability studies and stabilization approaches are planned as explicit objectives of our future work.

5 | Experimental Section

5.1 | Chemicals and Materials

Commercial copper foam with a thickness of 1.6 mm was purchased from Xtra GmbH. The nickel target (purity 99.99%) and cobalt target (purity 99.95%) for sputtering were purchased from Alineason Materials Technology GmbH. Tri-Natriumphosphat-Dodecahydrat (for analysis EMSURE, Reag. Ph Eur) was purchased from Merck. Potassium hydroxide (analytical reagent grade) and Acetic acid glacial were purchased from Fischer Scientific U.K. limited. Potassium nitrate 99% for analytical purposes and sodium hydroxide were purchased from Grüssing GmbH. Hydrochloric acid Puriss. p.a. fuming ≥37% ACS reagent was purchased from Fluka Honeywell. Sodium hypochlorite was purchased from Th.Geyer. Sodium nitroprusside dihydrate (GR for analysis ACS, Reag. Ph Eur), Sulfamic acid ACS reagent, 99.3% and Sodium salicylate ReagentPlus, ≥99.5% (titration) were purchased from Sigma-Aldrich. N-(1-Naphthyl)-ethylenediamine dihydrochloride ≥99%, p.a. and sulfanilamide ≥99% were purchased from Carl Roth.

5.2 | Methods and Methodology

The copper foams were modified with the physical vapor deposition (sputtering) of nickel and cobalt metals. Sputtering was conducted using argon (Ar) as the carrier gas at a pressure of 1.2×10^{-2} mbar and a discharge power of 100 W in DC mode. For electrochemical tests, a H-cell as shown in Figure S1 was used. 14 mL 0.1 M KOH + 0.016 M (1000 ppm) nitrate was used as catholyte and 0.1 M KOH was used as anolyte with a bipolar membrane (thickness: 110–160 μm & reinforced with PEEK) from Quintech separating two compartments. All the electrochemical tests were performed using a Metrohm potentiostat and a Biologic potentiostat as per need. The products (NH_3, NO_3^-, and NO_2^-) were quantified in the electrolyte after electrochemical performance using UV–Vis spectroscopy. The quantification methods [46, 86] of NO_3^-, NH_3, and NO_2^- are explained in detail in Supporting Information (Figures S2, S3, and S4).

XPS measurements were carried out using an AXIS Supra+ spectrometer (Kratos Analytical Ltd.) equipped with a monochromatic Al Kα X-ray source ($h\nu$ = 1486.6 eV). The X-ray source was operated at 12 kV and 25 W. Throughout all measurements, the pressure in the analysis chamber was maintained below 9×10^{-8} mbar. The electrodes were mounted on double-sided carbon tape, which was electrically isolated from the metallic sample holder by means of nonconductive tape in order to minimize charging effects. Survey spectra were collected over a BE range from 1400 to 0 eV using a step size of 1.0 eV and a pass energy of 160 eV. High-resolution spectra of selected regions were recorded with a step size of 0.1 eV and a pass energy of 20 eV, averaging 30 scans per region with a scan time of 60 s per sweep. Data acquisition was performed using ESCApe, while data processing and peak fitting were carried out with CasaXPS (version 2.3.27 rev. 1.7). BEs were corrected for charging effects by referencing to the adventitious carbon C 1s peak at 284.8 eV.

EIS measurements were performed in the working electrolyte (0.016 M NO_3^- + 0.1 M KOH) at open-circuit potential, over a frequency range from 10 Hz to 100 KHz with an AC perturbation amplitude of 10 mV. The equivalent circuits used for fitting are shown in Figure S11, and the corresponding χ^2 values are now reported in the revised Supporting Information.

XRD patterns of the prepared catalyst samples were recorded using Cu Kα radiation on a Bruker D2 PHASER diffractometer over a 2θ range from 6° to 90° with a step size of 0.02°. The static contact angle measurements were performed on the samples placed on an ordinary glass substrate at room temperature with a water volume of 10 μL in a syringe dropped on the sample surface. Images of the drop are then captured by a DNT digimicro scale, digital microscope. SEM analysis was performed with a JEOL JSM-IT800 at accelerating voltage of 5 kV with the SE detector from JEOL, as well as a backscattered electron detector from Gatan. EDX analysis was performed at accelerating voltage of 15 kV with Octane Elect Super detector.

Acknowledgments

The authors gratefully acknowledge Niklas Lothmann for his support with the sputtering process and Tobias Storp for his assistance with the XRD measurements.

Open Access funding enabled and organized by Projekt DEAL.

Funding

This work was supported by the German Federal Ministry of Education and Research (BMBF) (FKZ 03SF0627B).

Conflicts of Interest

The authors declare no conflicts of interest.

Data Availability Statement

The data that support the findings of this study are available from the corresponding author upon reasonable request.

References

1. IEA, International Energy Agency, (Ammonia Technology Roadmap, 2021).

2. S. Ameen, B. Iqbal, and H. Ijaz, "A Review on Advances in Electrocatalytic N_2 Reduction to Ammonia," *International Journal of Current Engineering and Technology* 12, no. 02 (2022): 114–121.

3. X. Guo, Y. Zhu, and T. Ma, "Lowering Reaction Temperature: Electrochemical Ammonia Synthesis by Coupling Various Electrolytes and Catalysts," *Journal of Energy Chemistry* 26, no. 6 (2017): 1107–1116.

4. M. Yasir, Z. Zhao, M. Zeng, S. Shanmugam, and X. Zhang, "Recent Progress and Prospects in Electroreduction of Nitrogen to Ammonia in Non-Aqueous Electrolytes," *Current Opinion in Electrochemistry* 45 (2024): 101487.

5. T.-Y. An, S. Surendran, S. C. Jesudass, et al., "Promoting Electrochemical Ammonia Synthesis by Synergized Performances of Mo_2C-Mo_2N Heterostructure," *Frontiers in Chemistry* 11 (2023): 1122150.

6. M. C. Hatzell, "A Decade of Electrochemical Ammonia Synthesis," *ACS Energy Letters* 7, no. 11 (2022): 4132–4133.

7. Z. Xue, C. Sun, M. Zhao, et al., "Efficient Electrocatalytic Nitrogen Reduction to Ammonia on Ultrafine Sn Nanoparticles," *ACS Applied Materials & Interfaces* 13, no. 50 (2021): 59834–59842.

8. S. Smita Biswas, S. Chakraborty, A. Saha, and M. Eswaramoorthy, "Electrochemical Nitrogen Reduction to Ammonia Under Ambient Conditions: Stakes and Challenges," *Chemical Record* 22, no. 11 (2022): e202200139.

9. Z. Qiao, D. Johnson, and A. Djire, "Challenges and Opportunities for Nitrogen Reduction to Ammonia on Transitional Metal Nitrides via Mars-Van Krevelen Mechanism," *Cell Reports Physical Science* 2, no. 5 (2021): 100438.

10. S. Niu, W. Liu, K. Wang, et al., "Research Advancements in Self-Supporting Electrodes for the Electrocatalytic Reduction of Nitrate to Ammonia," *Chemical Engineering Journal* 531 (2026): 174003.

11. Y. Kohlhaas, Y. S. Tschauder, W. Plischka, et al., "Electrochemical Urea Synthesis," *Joule* 8, no. 6 (2024): 1579–1600.

12. P. Banerjee, P. Garai, N. C. Saha, S. Saha, P. Sharma, and A. K. Maiti, "A Critical Review on the Effect of Nitrate Pollution in Aquatic Invertebrates and Fish," *Water, Air, and Soil Pollution* 234, no. 6 (2023): 703.

13. S. Garcia-Segura, M. Lanzarini-Lopes, K. Hristovski, and P. Westerhoff, "Electrocatalytic Reduction of Nitrate: Fundamentals to Full-Scale Water Treatment Applications," *Applied Catalysis B: Environmental* 236 (2018): 546–568.

14. Z. Zhang, N. Zhang, J. Zhang, et al., "Critical Review in Electrocatalytic Nitrate Reduction to Ammonia towards a Sustainable Nitrogen Utilization," *Chemical Engineering Journal* 483 (2024): 148952.

15. Y. Pan, H.-M. Xu, H.-R. Zhu, C.-J. Huang, Z.-J. Zhang, and G.-R. Li, "Recent Advances in Electrocatalytic Reduction of Nitrate to Ammonia: Current Challenges, Resolving Strategies, and Future Perspectives," *Journal of Materials Chemistry A* 13, no. 27 (2025): 21181–21232.

16. S. Yin and Y. Wang, "Progress and Challenges in the Electrocatalytic Reduction of Nitrate to Ammonia," *Molecules* 30, no. 19 (2025): 3910.

17. S. Niu, J. Yang, L. Qian, et al., "Electrochemical Nitrate Reduction to Ammonia – Recent Progress," *ChemElectroChem* 10, no. 21 (2023): e202300419.

18. S. Bunea, K. Clemens, and A. Urakawa, "Electrified Conversion of Contaminated Water to Value: Selective Conversion of Aqueous Nitrate to Ammonia in a Polymer Electrolyte Membrane Cell," *ChemSusChem* 15, no. 2 (2022): e202102180.

19. D. Liu, L. Qiao, S. Peng, et al., "Recent Advances in Electrocatalysts for Efficient Nitrate Reduction to Ammonia," *Advanced Functional Materials* 33, no. 43 (2023): 2303480.

20. W. Qiu, Y. Liu, M. Xie, Z. Jin, P. Li, and G. Yu, "Structural Engineering of Catalysts for Ammonia Electrosynthesis from Nitrate: Recent Advances and Challenges," *EES Catalysis* 2, no. 1 (2024): 202–219.

21. K. Zhang, X. Zou, Y. Liu, X. Zhang, and L. An, "Progress and Perspectives in the Electroreduction of Low-Concentration Nitrate for Wastewater Management," *iScience* 28, no. 1 (2025): 111687.

22. Y. Xie, M. de Ras, J. Zhao, et al., "Electrochemical Reduction of Nitrate to Hydroxylamine on Gold Electrode," *Chemical Communications* 60, no. 78 (2024): 10918–10921.

23. L. Bai, F. Franco, J. Timoshenko, et al., "Electrocatalytic Nitrate and Nitrite Reduction toward Ammonia Using Cu_2O Nanocubes: Active Species and Reaction Mechanisms," *Journal of the American Chemical Society* 146, no. 14 (2024): 9665–9678.

24. Y. Dang, R. Zhang, S. Ren, et al., "Balancing Active Hydrogen and NO_2− for Interfacial Tandem Nitrate Electrocatalysis to Ammonia," *Chemical Engineering Journal* 520 (2025): 166370.

25. J. Li, G. Zhan, J. Yang, et al., "Efficient Ammonia Electrosynthesis from Nitrate on Strained Ruthenium Nanoclusters," *Journal of the American Chemical Society* 142, no. 15 (2020): 7036–7046.

26. H. Liu, X. Lang, C. Zhu, et al., "Efficient Electrochemical Nitrate Reduction to Ammonia with Copper-Supported Rhodium Cluster and Single-Atom Catalysts," *Angewandte Chemie* 61, no. 23 (2022): e202202556.

27. Y. Hu, J. Liu, W. Luo, et al., "Alloying Pd with Ru Enables Electroreduction of Nitrate to Ammonia with ∼100% Faradaic Efficiency over a Wide Potential Window," *Chemical Science* 15, no. 21 (2024): 8204–8215.

28. G. Dima, A. de Vooys, and M. Koper, "Electrocatalytic Reduction of Nitrate at Low Concentration on Coinage and Transition-Metal Electrodes in Acid Solutions," *Journal of Electroanalytical Chemistry* 554 (2003): 15–23.

29. L. Huang, P. Zhang, X. Ge, et al., "Efficient Neutral Nitrate-to-Ammonia Electrosynthesis Using Synergistic Ru-Based Nanoalloys on Nitrogen-Doped Carbon," *Nano-Micro Letters* 18, no. 1 (2026): 66.

30. W. Qiu, M. Xie, P. Wang, et al., "Size-Defined Ru Nanoclusters Supported by TiO_2 Nanotubes Enable Low-Concentration Nitrate Electroreduction to Ammonia with Suppressed Hydrogen Evolution," *Small* 19, no. 30 (2023): e2300437.

31. X. Fu, X. Zhao, X. Hu, et al., "Alternative Route for Electrochemical Ammonia Synthesis by Reduction of Nitrate on Copper Nanosheets," *Applied Materials Today* 19 (2020): 100620.

32. Z.-Y. Wu, M. Karamad, X. Yong, et al., "Electrochemical Ammonia Synthesis via Nitrate Reduction on Fe Single Atom Catalyst," *Nature Communications* 12, no. 1 (2021): 2870.

33. E. Pérez-Gallent, M. C. Figueiredo, I. Katsounaros, and M. T. Koper, "Electrocatalytic Reduction of Nitrate on Copper Single Crystals in Acidic and Alkaline Solutions," *Electrochimica Acta* 227 (2017): 77–84.

34. L. Li, Y. Yun, Y. Zhang, Y. Huang, and Z. Xu, "Electrolytic Reduction of Nitrate on Copper and Its Binary Composite Electrodes," *Journal of Alloys and Compounds* 766 (2018): 157–160.

35. Y. Wang, A. Xu, Z. Wang, et al., "Enhanced Nitrate-to-Ammonia Activity on Copper-Nickel Alloys via Tuning of Intermediate Adsorption," *Journal of the American Chemical Society* 142, no. 12 (2020): 5702–5708.

36. S. Lombardi, S. Mostoni, L. Mirizzi, et al., "Design Strategies to Enhance Copper Electrocatalytic Performance for Nitrate-to-Ammonia Electroreduction," *ChemElectroChem* 12, no. 7 (2025): e202400482.

37. Y. Wang, W. Zhou, R. Jia, Y. Yu, and B. Zhang, "Unveiling the Activity Origin of a Copper-Based Electrocatalyst for Selective Nitrate Reduction to Ammonia," *Angewandte Chemie* 59, no. 13 (2020): 5350–5354.

38. Y. Zhang, X. Chen, W. Wang, L. Yin, and J. C. Crittenden, "Electrocatalytic Nitrate Reduction to Ammonia on Defective Au1Cu (111) Single-Atom Alloys," *Applied Catalysis B: Environmental* 310 (2022): 121346.

39. W. Fu, Y. Du, J. Jing, C. Fu, and M. Zhou, "Highly Selective Nitrate Reduction to Ammonia on CoO/Cu Foam via Constructing Interfacial Electric Field to Tune Adsorption of Reactants," *Applied Catalysis B: Environmental* 324 (2023): 122201.

40. L. Z. Dai, G. Y. Yong, W. N. Gan, et al., "Self-Reconstructed Cu_2O/Co_3O_4@NC Heterostructured Catalyst for Efficient Tandem Electrocatalytic Conversion of Nitrate to Ammonia," *Chemical Engineering Journal* 521 (2025): 166680.

41. Y. Ren, J. Wang, L. Yang, et al., "Single-Atom Cu and Zn Vacancy Synergy in NiFe-LDH Boosts Metal-Support Interaction for High-Efficiency Nitrate-to-Ammonia Electroreduction," *Environmental Science & Technology* 59, no. 22 (2025): 11414–11425.

42. J. M. McEnaney, S. J. Blair, A. C. Nielander, et al., "Electrolyte Engineering for Efficient Electrochemical Nitrate Reduction to Ammonia on a Titanium Electrode," *ACS Sustainable Chemistry & Engineering* 8, no. 7 (2020): 2672–2681.

43. Y. Han, S. Li, X. Li, J. Ma, J. Ping, and Y. Sun, "Study on Process Parameters of Magnetron Sputtering Titanium Coating in Deep Porous Structures," *ACS Omega* 9, no. 12 (2024): 14551–14557.

44. X. Wang, L. Xin, F. Wang, S. Zhu, H. Wei, and X. Wang, "Influence of Sputtered Nanocrystalline Coating on Oxidation and Hot Corrosion of a Nickel-Based Superalloy M951," *Journal of Materials Science & Technology* 30, no. 9 (2014): 867–877.

45. K. Singh, N. Krishnamurthy, and A. K. Suri, "Adhesion and Wear Studies of Magnetron Sputtered NbN Films," *Tribology International* 50 (2012): 16–25.

46. X. Wei, R. Feng, S. Albarqawi, et al., "Sputter-Deposited Ruthenium Nitrides for Electrochemical Nitrogen Fixation to Ammonia under Ambient Conditions," *ACS Applied Materials & Interfaces* 18, no. 6 (2026): 9939–9951.

47. W. Darenfad, N. Guermat, and K. Mirouh, "Effect of Co-Doping on Structural, Morphological, Optical and Electrical Properties of p-Type CuO Films," *Journal of Nano- and Electronic Physics* 15, no. 6 (2023): 06009–06009-6.

48. H. D. Omar, "The Analysis of Copper-Iron Metallic Mixture by Means of XRD and XRF," *International Letters of Chemistry, Physics and Astronomy* 64 (2016): 130–134.

49. S. G. Kandalkar, J. L. Gunjakar, and C. D. Lokhande, "Preparation of Cobalt Oxide Thin Films and Its use in Supercapacitor Application," *Applied Surface Science* 254, no. 17 (2008): 5540–5544.

50. H. D. Omar, "Intensity Correction and Pole Figure Measurement of Copper Metallic by XRD," *Journal of Basic & Applied Sciences* 12 (2016): 320–322.

51. G. Patel, F. Ganss, R. Salikhov, et al., "Structural and Magnetic Properties of Thin Cobalt Films with Mixed Hcp and Fcc Phases," *Physical Review B* 108, no. 18 (2023): 84429.

52. S. Jung, D. K. Nandi, S. Yeo, et al., "Phase-Controlled Growth of Cobalt Oxide Thin Films by Atomic Layer Deposition," *Surface and Coatings Technology* 337 (2018): 404–410.

53. J.-H. Kim, H.-J. Kil, S. Lee, J. Park, and J.-W. Park, "Interfacial Delamination at Multilayer Thin Films in Semiconductor Devices," *ACS Omega* 7, no. 29 (2022): 25219–25228.

54. S. Massl, W. Thomma, J. Keckes, and R. Pippan, "Investigation of Fracture Properties of Magnetron-Sputtered TiN Films by Means of a FIB-Based Cantilever Bending Technique," *Acta Materialia* 57, no. 6 (2009): 1768–1776.

55. S. Yu, L. Ma, L. He, and Y. Ni, "Hierarchical Crack Patterns of Metal Films Sputter Deposited on Soft Elastic Substrates," *Physical Review E* 100, no. 5 (2019): 52804.

56. M. Galbiati, A. C. Stoot, D. M. A. Mackenzie, P. Bøggild, and L. Camilli, "Real-Time Oxide Evolution of Copper Protected by Graphene and Boron Nitride Barriers," *Scientific Reports* 7 (2017): 39770.

57. T. Ghodselahi, M. A. Vesaghi, A. Shafiekhani, A. Baghizadeh, and M. Lameii, "XPS Study of the Cu@Cu2O Core-Shell Nanoparticles," *Applied Surface Science* 255, no. 5 (2008): 2730–2734.

58. V. Hayez, A. Franquet, A. Hubin, and H. Terryn, "XPS Study of the Atmospheric Corrosion of Copper Alloys of Archaeological Interest," *Surface and Interface Analysis* 36, no. 8 (2004): 876–879.

59. M. C. Biesinger, "Advanced Analysis of Copper X-Ray Photoelectron Spectra," *Surface & Interface Analysis* 49, no. 13 (2017): 1325–1334.

60. P. D. Kirsch and J. G. Ekerdt, "Chemical and Thermal Reduction of Thin Films of Copper (II) Oxide and Copper (I) Oxide," *Journal of Applied Physics* 90, no. 8 (2001): 4256–4264.

61. F. S. Gard, G. Duffo, P. Bergamasco, and E. Forlerer, "X-Ray Photoelectron Spectroscopy on 1-Peso and 2-Pesos of the Argentine Republic," *Applied Surface Science* 436 (2018): 720–731.

62. G. Fierro, M. L. Jacono, M. Inversi, R. Dragone, and P. Porta, "TPR and XPS Study of Cobalt-Copper Mixed Oxide Catalysts: Evidence of a Strong Co-Cu Interaction," *Topics in Catalysis* 10 (2000): 39–48.

63. K. Ismail and W. Badawy, "Electrochemical and XPS Investigations of Cobalt in KOH Solutions," *Journal of Applied Electrochemistry* 30 (2000): 1303–1311.

64. L. Lukashuk, N. Yigit, R. Rameshan, et al., "Operando Insights into CO Oxidation on Cobalt Oxide Catalysts by NAP-XPS, FTIR, and XRD," *ACS Catalysis* 8, no. 9 (2018): 8630–8641.

65. Y. Han, S. Axnanda, E. J. Crumlin, et al., "Observing the Electrochemical Oxidation of Co Metal at the Solid/Liquid Interface Using Ambient Pressure X-Ray Photoelectron Spectroscopy," *Journal of Physical Chemistry B* 122, no. 2 (2018): 666–671.

66. M. C. Biesinger, B. P. Payne, A. P. Grosvenor, L. W. Lau, A. R. Gerson, and R. S. Smart, "Resolving surface chemical states in XPS analysis of first row transition metals, oxides and hydroxides: Cr, Mn, Fe, Co and Ni," *Applied Surface Science* 257, no. 7 (2011): 2717–2730.

67. C. Leygraf, I. O. Wallinder, J. Tidblad, and T. Graedel, "*Atmospheric Corrosion*," (John Wiley & Sons, Inc, 2016).

68. J. Dupin, D. Gonbeau, P. Vinatier, and A. Levasseur, "Systematic XPS Studies of Metal Oxides, Hydroxides and Peroxides," *Physical Chemistry Chemical Physics* 2 (2000): 1319–1324.

69. D. S. Hall, C. Bock, and B. R. MacDougall, "The Electrochemistry of Metallic Nickel: Oxides, Hydroxides, Hydrides and Alkaline Hydrogen Evolution," *Journal of The Electrochemical Society* 160, no. 3 (2013): F235–F243.

70. K. Zhang, P. Sun, Y. Huang, et al., "Electrochemical Nitrate Reduction to Ammonia on CuCo Nanowires at Practical Level," *Advanced Functional Materials* 34, no. 44 (2024): 2405179.

71. D. Miao, J. Li, J. Ren, and Z. Chen, "Exploring the Potential of Ni-Based Hydrogen Evolution Catalysts in Anion Exchange Membrane Water Electrolyzer," *Advanced Materials* 38 (2026): e20491.

72. L. Huo, C. Jin, K. Jiang, Q. Bao, Z. Hu, and J. Chu, "Applications of Nickel-Based Electrocatalysts for Hydrogen Evolution Reaction," *Advanced Energy and Sustainability Research* 3, no. 4 (2022): 2100189.

73. C. Deng, C. Qi, X. Wu, G. Jing, and H. Zhao, "Unveiling the Relationship between Structural Evaluation and Catalytic Performance of InOOH during Electroreduction of CO_2 to Formate," *Green Carbon* 2, no. 1 (2024): 124–130.

74. Z. Zhang, B. Ge, M. Liu, et al., "Synergistic Cu_2O@$Ni(OH)_2$ Core-Shell Electrocatalyst for High-Efficiency Nitrate Reduction to Ammonia," *ACS Applied Materials & Interfaces* 17, no. 18 (2025): 26501–26510.

75. L. He, F. Yao, Y. Zhong, et al., "Achieving High-Performance Electrocatalytic Reduction of Nitrate by N-Rich Carbon-Encapsulated Ni-Cu Bimetallic Nanoparticles Supported Nickel Foam Electrode," *Journal of Hazardous Materials* 436 (2022): 129253.

76. W. Cao, X. He, X. Cai, Q. Hu, J. Zhang, and F. Yang, "Electrochemical Nitrate Reduction to Ammonia Using Fe-Doped TiO_2 Nanoparticles as Electrocatalysts: The Synergistic Contribution from Fe and Oxygen Vacancy," *Journal of Alloys and Compounds* 1036 (2025): 181654.

77. L. Thapa, S. Mallobarman, and C. R. Raj, "Paired Electrocatalysis: Nitrate Reduction to Ammonia Coupled with Anodic Upcycling of Biomass and Plastic Waste," *ACS Applied Materials & Interfaces* 17, no. 42 (2025): 57803–57838.

78. J. Wang, C. Cai, Y. Wang, et al., "Electrocatalytic Reduction of Nitrate to Ammonia on Low-Cost Ultrathin CoO x Nanosheets," *ACS Catalysis* 11, no. 24 (2021): 15135–15140.

79. K.-H. Kim, H. Lee, X. Huang, et al., "Energy-Efficient Electrochemical Ammonia Production from Dilute Nitrate Solution," *Energy & Environmental Science* 16, no. 2 (2023): 663–672.

80. O. Q. Carvalho, R. Marks, H. K. K. Nguyen, et al., "Role of Electronic Structure on Nitrate Reduction to Ammonium: A Periodic Journey," *Journal of the American Chemical Society* 144, no. 32 (2022): 14809–14818.

81. D. Reyter, D. Bélanger, and L. Roué, "Study of the Electroreduction of Nitrate on Copper in Alkaline Solution," *Electrochimica Acta* 53, no. 20 (2008): 5977–5984.

82. G. Wang, Z. Chen, J. Xie, et al., "Recent Trends and Prospects in Electrochemical Nitrate Reduction to Ammonia with an Emphasis on Cobalt Catalysts," *Coordination Chemistry Reviews* 539 (2025): 216751.

83. C. Liu, C. Yang, W. Zhang, and Y. Li, "Promoting $*NO_2$ Hydrogeneration on Cobalt-Doped Copper Oxides for Selective Ammonia Electrosynthesis from Nitrate," *ChemSusChem* 18, no. 11 (2025): e202500017.

84. C. Costentin and J.-M. Savéant, "Electrochemical Capacitive Charging in Porous Materials. Discriminating between Ohmic Potential Drop and Counterion Diffusion," *ACS Applied Energy Materials* 2, no. 7 (2019): 4981–4986.

85. V. Ramadesigan, R. N. Methekar, F. Latinwo, R. D. Braatz, and V. R. Subramanian, "Optimal Porosity Distribution for Minimized Ohmic Drop across a Porous Electrode," *Journal of the Electrochemical Society* 157, no. 12 (2010): A1328–A1334.

86. R. B. Willis, M. E. Montgomery, and P. R. Allen, "Improved Method for Manual, Colorimetric Determination of Total Kjeldahl Nitrogen Using Salicylate," *Journal of Agricultural and Food Chemistry* 44, no. 7 (1996): 1804–1807.

Supporting Information

Additional supporting information can be found online in the Supporting Information section.